OPEN ACCESS
Journal of Innovative Optical Health Sciences
Vol. 15, No. 6 (2022) 2240009 (13 pages)

DOI: 10.1142/S1793545822400090

World Scientific
www.worldscientific.com

A novel BODIPY-based nano-photosensitizer with aggregation-induced emission for cancer photodynamic therapy

Yuting Zhang[*,†], Guojing Li[‡], Jiong Li[†,§,‖,††], Ming Wu[†], Xiaolong Liu[*,†] and Jingfeng Liu[*,†,¶,**,††]

[*]*School of Life Sciences, Fujian Agriculture and Forestry University*
Fuzhou 350002, P. R. China

[†]*The United Innovation of Mengchao Hepatobiliary Technology Key Laboratory of Fujian Province*
Mengchao Hepatobiliary Hospital of Fujian Medical University
Fuzhou 350025, P. R. China

[‡]*Key Laboratory for Green Chemical Process of the Ministry of Education*
School of Chemical Engineering and Pharmacy
Wuhan Institute of Technology, Wuhan 430205, P. R. China

[§]*Key Laboratory of Biomedical Information Engineering of Ministry of Education*
Institute of Biomedical Photonics and Sensing
School of Life Science and Technology
Xi'an Jiaotong University, Xi'an 710049, P. R. China

[¶]*Fujian Cancer Hospital and Fujian Medical University Cancer Hospital*
Fuzhou 350014, P. R. China
[‖]*ljiong726101@163.com*
[**]*drjingfeng@126.com*

Received 28 May 2022
Revised 29 July 2022
Accepted 9 August 2022
Published 15 September 2022

The discovery of aggregation-induced emission (AIE) effect provides opportunities for the rapid development of fluorescence imaging-guided photodynamic therapy (PDT). In this work, a boron dipyrromethene (BODIPY)-based photosensitizer (ET-BDP-O) with AIE characteristics was developed, in which the two linear arms of BODIPY group were linked with triphenylamine to form an electron Donor–Acceptor–Donor (D–A–D) architecture while side chain was equipped with triethylene glycol group. ET-BDP-O was able to directly self-assemble into nanoparticles (NPs) without supplement of any other matrices or stabilizers due to its amphiphilic property.

[††]Corresponding authors.

The as-prepared ET-BDP-O NPs had an excellent colloid stability with the size of 125 nm. Benefiting from the AIE property, ET-BDP-O NPs could generate strong fluorescence and reactive oxygen species under light-emitting diode light irradiation (60 mW/cm^2). After internalized in cancer cells, ET-BDP-O NPs were able to emit bright red fluorescence signal for bioimaging. In addition, the cell viability assay demonstrated that the ET-BDP-O NPs exhibited excellent photo-cytotoxicity against cancer cells, while negligible cytotoxicity under dark environment. Thus, ET-BDP-O NPs might be regarded as a promising photosensitizer for fluorescence imaging-guided PDT in future.

Keywords: BODIPY-based nano-photosensitizer; aggregation-induced emission (AIE); fluorescence imaging; photodynamic therapy.

1. Introduction

As a minimally invasive therapeutic modality, photodynamic therapy (PDT) has been extensively studied in cancers owing to the high specificity, enhanced controllability and low side effects.[1,2] The therapeutic effect of PDT mainly depends on the production of reactive oxygen species (ROS) from photosensitizer (PS). In brief, the molecular mechanisms of PDT mainly consist of two processes: (i) PS molecules exposed under the light sources (lasers and incandescent light sources) undergo a transition from the ground state (S_0) to the excited singlet state (S_1), and then to the triplet state (T_1) *via* intersystem crossing; (ii) PS in the triplet state would interact with its surrounding molecules, especially O_2 molecules, to generate various types of ROS, which can cause irreversible damages of DNA and proteins to induce cancer cell apoptosis or necrosis, thereby achieving favorable therapeutic effects.[2–7]

As one of the key elements, PS plays a crucial role in PDT and even determines the outcomes of treatment. PS used in PDT first appeared in 1970s, mainly classified in porphyrins and their derivatives.[2,8] Porphyrin derivatives are a class of heterocyclic organic molecules with excellent $^1O_2$ generation efficiency, fluorescence property and special affinity for cancer cells that have been widely studied and used as PS for clinical treatment.[9,10] For example, the first-generation PS (Photofrin®, a porphyrin derivative) approved by FDA has been widely applied in the treatment of esophageal cancer, bladder cancer, gastric cancer, etc.[1,2,11] In order to surmount the disadvantages of Photofrin® during PDT, including cumbersome synthesis steps, poor aqueous solubility, long residence time in normal tissue, severe photosensitivity of the skin and low accumulation of target site, researchers have successively developed the second-generation porphyrin PS of Hemoporfin® (chlorin, bacteriochlorin and phthalocyanine) and the third-generation PS.[9,12] The so-called third-generation PS was designed with specific recognition and target function rely on the modification of second-generation PS with peptides, monoclonal antibodies, liposomes, polysaccharides and folic acid.[13,14] However, porphyrin PSs are always plagued by photobleaching and poor photostability, leading to severely compromised photosensitization and unsatisfactory PDT effect.[7,10,15]

Recently, boron dipyrromethene (BODIPY) and its derivatives have drawn increasing attention as PDT agents with advantages of large molar extinction coefficients, enhanced photophysical stability and high quantum yields.[16–19] Moreover, BODIPY can be modified with different moieties to realize active targeting or responsive imaging and therapy.[20,21] Unfortunately, PSs with planar structures, including BODIPY and porphyrin PSs, usually suffer from the aggregation-caused quenching (ACQ) effect due to strong π–π interaction, whereas the extended delocalized aromatic π electron in PSs is necessary.[22] The ACQ effect of PSs not only has an adverse influence on ROS production, but also reduces the intensity of fluorescence signal when PSs accumulate at the lesions with a high concentration or aggregate states.[23,24] Besides, most BODIPY derivatives can be effectively excited to S_1, but subsequently have the poor ability of intersystem crossing to T_1, which also hinder the potential of ROS production and impair the therapeutic effect of PDT.[25] Therefore, the development of BODIPY-based PSs with excellent fluorescence property and enhanced intersystem crossing capability is enormously helpful for the

improvement of PDT-related therapeutic paradigm.

Aggregation-induced emission (AIE) fluorogens provide a new insight for the development of PSs. AIE-based PSs are able to achieve intensified fluorescence properties and ROS generation capability in the aggregate state due to the prohibition of energy dissipation and restriction of intramolecular motion.[26] Additionally, introducing an D–A–D architecture to the AIE-based PSs can not only effectively reduce the S_1–T_1 energy gap to boost intersystem crossing for photosensitization improvement, but also redshift the absorption and fluorescence emission wavelength for improved penetration depth, contributing to the imaging and therapy of deep tissue tumors.[7]

In this work, we introduced 4-ethynyl triphenylamine (ET, a derivative of triphenylamine (TPA)) as the electron donor into BODIPY core with triethylene glycol modification to develop a novel AIE-based PS (denoted as ET-BDP-O) with D–A–D structure. The ET-BDP-O not only exhibited excellent photophysical properties, but also can self-assemble into nanoparticles (NPs) relying on the introduction of triethylene glycol group via nanoprecipitation method. Further characterizations and *in vitro* experiments demonstrated that the ET-BDP-O NPs with good colloidal stability, bright fluorescence emission, excellent ROS generation and killing effect, have considerable potential for fluorescence imaging-guided PDT therapy as a novel AIE-based PS agent.

2. Materials and Methods

2.1. *Materials*

Triethylene glycol monoethyl ether, toluenesulfonyl chloride, 4-hydroxybenzaldehyde, 2,4-dimethylpyrrole, 4,6-diamidino-2-phenylindole (DAPI) were purchased from Aladdin (Shanghai, China). 4-Ethynyl triarylamine (E-TPA) was purchased from Achem-block (Beijing, China). Singlet oxygen sensor green (SOSG) reagent was acquired from Meilunbio (Dalian, China). Cell Counting Kit-8 (CCK-8) was acquired from Dojindo Molecular Technologies (Tokyo, Japan). 2,7-Dichlorodihydrofluorescein diacetate (DCFH-DA) and Calcein-AM were obtained from J&K Scientific. Deionized water (18.2 MΩ cm) was obtained using a Milli-Q Gradient System (Millipore Corporation, Bedford, MA, USA) and used for all the experiments. All other chemicals, if not specified, were commercially available and used as received.

2.2. *Cell lines and culture*

The murine breast cancer line 4T1 cells were obtained from ATCC (Manassas, VA), and cultured in Dulbecco's modified Eagle medium (DMEM) supplemented with 10% fetal bovine serum and 1% penicillin–streptomycin solution in a 5% CO_2 humidity incubator at 37°C.

2.3. *Synthesis of compounds 1 and 2*

Triethylene glycol monoethyl ether (5.00 g, 28.06 mmol) in tetrahydrofuran (THF, 10 mL) and NaOH (6.25 mmol) in water (9.2 mL) were mixed and stirred at 0°C. After 15 min, toluenesulfonyl chloride (6.90 g, 36.20 mmol) in THF was added dropwise and stirred for another 2 h. After removing THF under reduced pressure, the resulting mixture was dissolved in dichloromethane (DCM) and washed with ice water for three times. The solvent was then dried with anhydrous Na_2SO_4 and removed under reduced pressure to afford colorless oil (defined as compound **1**). ^{1}H NMR (400 MHz, $CDCl_3$): δ (ppm) 7.78 (d, $J = 8.4$ Hz, 2H), 7.32 (d, $J = 8.4$ Hz, 2H), 4.14 (t, $J = 4.8$ Hz, 2H), 3.66 (t, $J = 4.8$ Hz, 2H), 3.61–3.53 (m, 8H), 3.49 (q, $J = 6.9$ Hz, 2H), 2.42 (s, 3H), 1.18 (t, $J = 7$ Hz, 3H).

Compound **1** (25.0 mmol) was reacted with 4-hydroxybenzaldehyde (25.0 mmol) in 70 mL of *N*,*N*-dimethylformamide containing 6.9 g of K_2CO_3 (50 mmol) under stirring in a nitrogen atmosphere at 90°C for 18 h. Next, the solvent was removed under reduced pressure, and the resulting mixture was dissolved in DCM and washed with ice water for three times. The organic layer was then dried with anhydrous Na_2SO_4 and evaporated in vacuum. The crude product was purified by silica gel column chromatography (ethylacetate/petroleum ether = 2:3) to give compound **2** as a light yellow oil. ^{1}H NMR (400 MHz, $CDCl_3$): δ (ppm) 7.80 (d, $J = 8.7$ Hz, 2H), 6.99 (d, $J = 8.7$ Hz, 2H), 4.19 (t, 2H), 3.87 (t, $J = 4.0$ Hz, 2H), 3.71 (m, $J = 3.4$ Hz, 2H), 3.68–3.60 (m, 4H), 3.56 (m, 2H), 3.49 (t, $J = 7.0$ Hz, 2H), 1.18 (t, $J = 7$ Hz, 3H).

2.4. *Synthesis of ET-BDP-O*

ET-BDP-O was synthesized according to the previously reported method.[27,28] Briefly, compound **2** (1 mmol) and 2,4-dimethylpyrrole (2.5 mol) were dissolved in 40 mL of anhydrous DCM (40 mL). After stirred for 30 min. trifluoroacetic acid (10 μL) and 2,3-dichloro-5,6-dicyano-1,4-benzoquinone (DDQ) were successively added into the mixture under stirring for another 12 h or 2 h, respectively. Afterwards, trimethylamine (10 mmol) was added to quench the reaction for 30 min. Then, boron trifluoride diethyl etherate (BF_3-OEt_2, 10 mmol) was added dropwise into the solution for another 3 h of reaction. The desired product (BDP-O) was purified from silica gel column chromatography ($DCM/CH_3OH = 90:1$).

BDP-O (250 mg, 0.5 mmol) and *N*-iodosuccinimide (NIS, 450 mg, 2 mmol) were dissolved in 15 mL of anhydrous DCM (15 mL). After stirred at room temperature for 1 h, the mixture was washed with saturated Na_2SO_3 aqueous solution and dried over anhydrous Na_2SO_4. The crude product was purified by silica gel column chromatography ($DCM/CH_3OH = 120:1$) to yield the product of II-BDP-O. Finally, II-BDP-O (200 mg, 0.266 mmol) and E-TPA (179 mg, 0.665 mmol) were added to a 50 mL double-necked flask. Under a N_2 atmosphere, $PdCl_2(PPh_3)_2$ (18.7 mg, 0.027 mmol), CuI (5.1 mg, 0.027 mmol) and THF/Et_3N (3:1) were added and stirred for 12 h at 80°C, followed by evaporation under reduced pressure. The crude product was purified by silica gel column chromatography ($CH_2Cl_2/CH_3OH = 90:1$) to give the final product of ET-BDP-O as dark blue solid.

2.5. *Preparation of ET-BDP-O NPs*

ET-BDP-O (4 mg) dissolved in 1.5 mL of THF was added dropwise into 15 mL of ddH_2O under a water bath sonicator. After sonication for 2 min, the mixture was stirred overnight to evaporate THF completely. The ET-BDP-O NPs were obtained directly and stored at 4°C for further usage. The concentration of ET-BDP-O NPs solution was 81.78 μg/mL, as measured by its absorbance at 600 nm.

2.6. *Characterization of ET-BDP-O NPs*

The morphology of ET-BDP-O NPs was characterized by transmission electron microscopy (TEM, FEI Company, Hillsboro, OR). Dynamic light scattering (DLS) measurements were executed on a Zetasizer Nano ZS90 equipment (Malvern Instruments, Southborough, MA). The UV–Vis absorbance and fluorescence spectrum were measured by a SpectraMax M5 microplate reader (Molecular Devices, USA) and a Cary Eclipse fluorescence spectrophotometer (Agilent Technologies, Malaysia), respectively.

2.7. *ROS generation*

2,2,6,6-Tetramethylpiperidine (TEMP) and 5,5-dimethyl-1-pyrroline *N*-oxide (DMPO) were, respectively, used to spin trap $^1O_2$ and ·OH, and the corresponding electron paramagnetic resonance (EPR) spectra were recorded to monitor the ROS generation of ET-BDP-O treated with 592 nm light-emitting diode (LED) lamp (60 mW/cm^2) for 10 min.

Besides, SOSG was also used to assess ROS generation of ET-BDP-O NPs. 1 μL of SOSG (5 mM) in methanol was added into ET-BDP-O NPs (1 mL in water) at different concentrations (0, 1, 3, 5 and 7 μg/mL). Next, the mixture was irradiated under a 592 nm LED lamp at a power density of 60 mW/cm^2 for different times (0, 2, 4, 6, 8 and 10 min). The fluorescence spectra of the mixtures between 500 nm and 650 nm were recorded using a Cary Eclipse fluorescence spectrophotometer at 488 nm wavelength excitation. The value of F_t/F_0 at 527 nm was further calculated to evaluate the ROS generation efficiency (F_0: initial fluorescence intensity; F_t: fluorescence intensity after irradiation for different times).

2.8. *Cellular uptake*

4T1 cells were seeded in confocal dishes at a density of 1.5×10^5 cells and cultured for 12 h. Then, the original medium was replaced with fresh medium containing ET-BDP-O NPs (15 μg/mL). After further incubation for a certain time period (6, 12 or 24 h), the cells in confocal dishes were washed with phosphate-buffered saline (PBS) for three times, fixed with 4% paraformaldehyde solution for 30 min, stained with DAPI for 15 min and final observed under a confocal laser scanning microscope (CLSM, Zeiss LSM780).

2.9. *In vitro cytotoxicity assay*

The cytotoxicity of ET-BDP-O NPs to 4T1 cells was determined by the CCK-8 assay. Briefly, 4T1 cells (1×10^4 cells/well) were inoculated in a 96-well plate and cultured for 12 h. Next, the cells were incubated with different concentrations of ET-BDP-O NPs (0, 5, 15, 25 and 35 μg/mL) for another 24 h. Then, the cells were exposed under a 592 nm LED lamp (60 mW/cm^2) for 10 min. After another 24 h of incubation, the cell viability was measured by CCK-8 assay and calculated from the following formula:

$$\text{Cell viability (\%)} = (A_1 - A_{\text{blank}})/(A_0 - A_{\text{blank}}) \times 100\%. \quad (1)$$

Herein, A_{blank} is the absorbance value of the CCK-8 medium solution itself at 450 nm. A_1 is the absorbance value of the cells treated with different concentrations of ET-BDP-O NPs. A_0 is the absorbance value of cells without treatment. All samples were performed in five parallel repeats.

Besides, Calcein-AM/propidium iodide (PI) staining was conducted to further investigate PDT effect of ET-BDP-O NPs. The 4T1 cells with aforementioned treatments were stained with Calcein-AM and PI for 30 min. After washing twice with PBS, the cells were observed and imaged by a fluorescence microscope (Zeiss Axio Vert.A1, Germany).

2.10. *Intracellular ROS detection*

ROS in 4T1 cells was detected by the DCFH-DA detection probe. 4T1 cells were seeded in a 96-well plate at the density of 1×10^4 cells and cultured for 12 h. Then, the cells were treated with ET-BDP-O NPs for another 24 h. After washed with PBS, the cells were incubated with DCFH-DA (100 μM) for 30 min. Subsequently, the cells were washed twice with PBS, replenished with fresh DMEM medium, and irradiated with a 592 nm LED lamp (60 mW/cm^2, 10 min). Finally, the cells were visualized and imaged by a fluorescence microscope (Zeiss Axio Vert.A1, Germany).

3. Results and Discussion

3.1. *Synthesis and characterization*

The synthetic route of ET-BDP-O is schematically illustrated in Fig. 1(a). Triethylene glycol monoethyl ether was grafted in the side chain of BODIPY to increase its water solubility. Meanwhile, the two linear arms were modified with TPA to form a D–A–D structure which could help the compound to decrease the energy bandgap and endow it with AIE property. In detail, compound **2** and pyrrole were mixed at room temperature, oxidized with DDQ and chelated with boron to obtain BODIPY host molecules (BDP-O) with side chain substituted with triethylene glycol chains. After iodinated reaction with NIS, the expected ET-BDP-O was obtained by Sonogashira coupling reaction between iodized BDP-O and E-TPA, using $PdCl_2(PPh_3)_2$ and CuI as catalysts. The chemical structures of ET-BDP-O were characterized by ^{1}H NMR (Fig. 1(b)), verifying the successful synthesis of this molecule.

3.2. *Preparation and characterization of ET-BDP-O NPs*

The ET-BDP-O NPs were prepared by self-assembly of ET-BDP-O via a nanoprecipitation method. TEM image demonstrated the formation of nanoscaled aggregates, which was in line with the results of DLS, as depicted in Figs. 2(a) and 2(b). The average hydrodynamic size (D_H) of ET-BDP-O NPs was 125 ± 0.9 nm with a small polydispersity index (PDI) value about 0.17, indicating a good dispersion of these NPs. Meanwhile, the zeta potential of ET-BDP-O NPs was measured to be -27.4 mV (Fig. 2(c)), contributing to stable colloid system via electrostatic repulsion among ET-BDP-O NPs. To further verify the stability, ET-BDP-O NPs were stored in aqueous solution for 6 days, the D_H values and corresponding PDI value of ET-BDP-O NPs were monitored and recorded by DLS. As displayed in Fig. 2(d), both of the D_H and PDI values do not have significant changes compared to the initial values, demonstrating a good colloidal stability of ET-BDP-O NPs in aqueous solution.

3.3. *Photophysical properties*

Optical characteristics are the fundamental properties of PSs. Then, we next investigated the absorption and fluorescence spectra of ET-BDP-O and ET-BDP-O NPs. As shown in Fig. 3(a), the UV–Vis absorption spectra of ET-BDP-O and ET-BDP-O NPs in aqueous solution were measured from

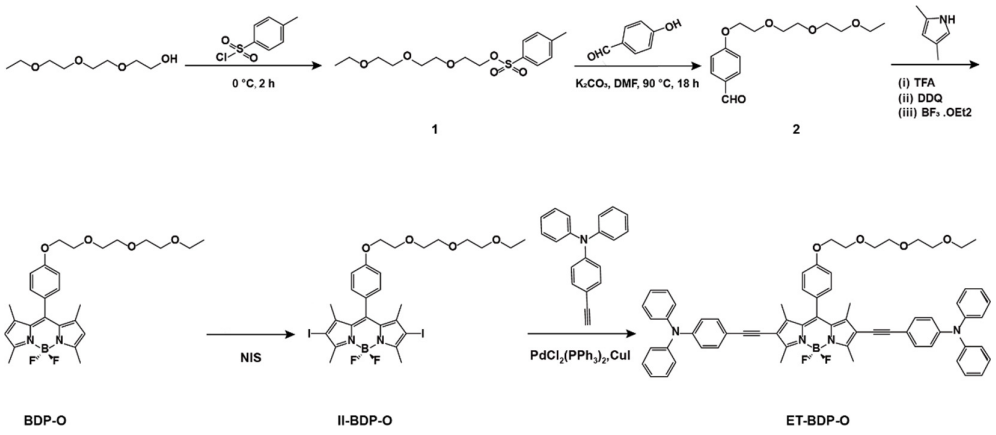

(a)

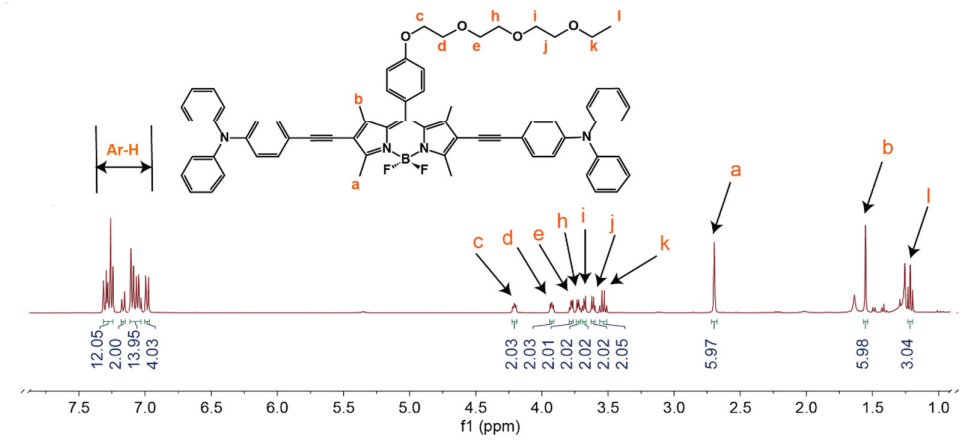

(b)

Fig. 1. Synthesis of ET-BDP-O. (a) Synthesis route of ET-BDP-O. (b) ^{1}H NMR spectra of ET-BDP-O in $CDCl_3$. Ar–H refers to H on the benzene.

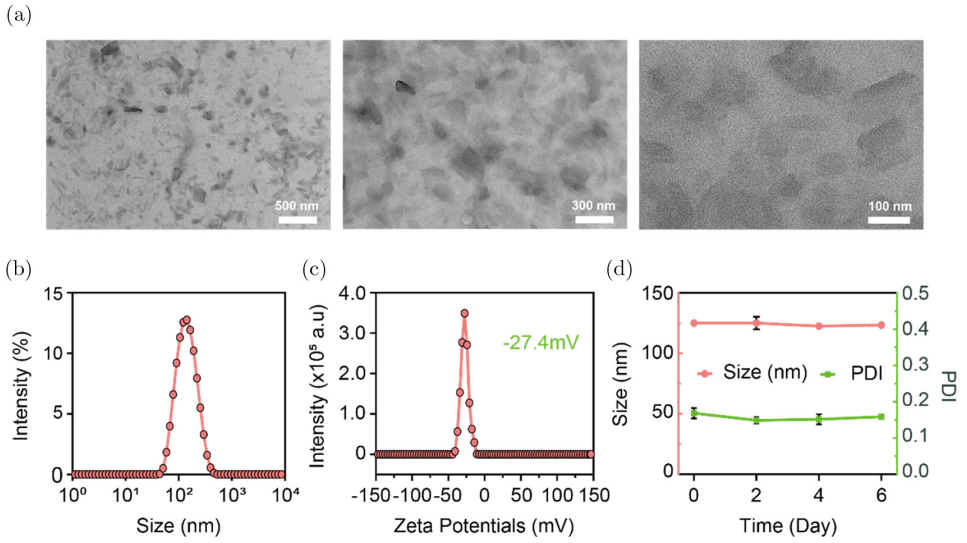

Fig. 2. Characterization of ET-BDP-O NPs. (a) TEM image of ET-BDP-O NPs. (b) DLS profile of ET-BDP-O NPs. (c) Zeta potential of ET-BDP-O NPs. (d) Size and PDI of ET-BDP-O NPs in aqueous solution.

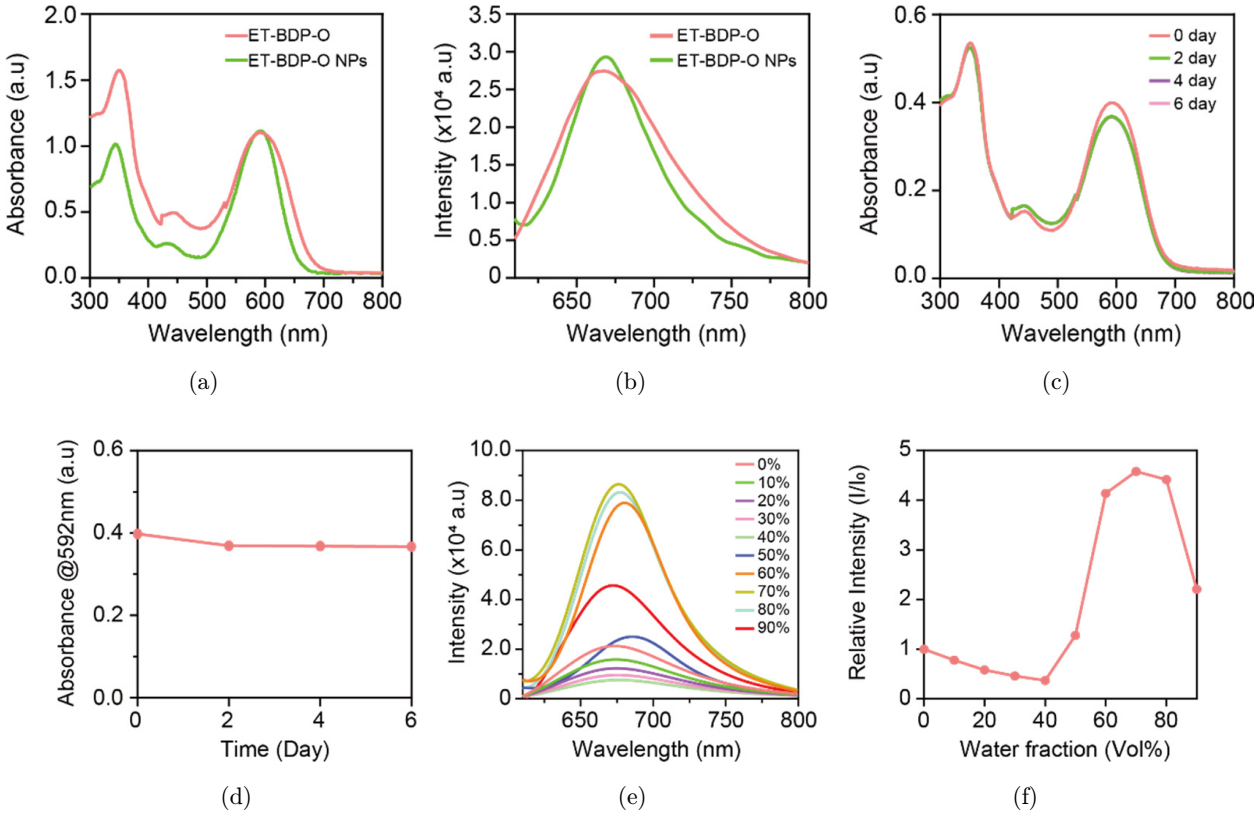

Fig. 3. The optical characteristics of ET-BDP-O and ET-BDP-O NPs. (a) UV–Vis absorption spectra of ET-BDP-O and ET-BDP-O NPs. (b) Fluorescence spectra of ET-BDP-O and ET-BDP-O NPs. (c) UV–Vis absorption of ET-BDP-O NPs stored in water for different days. (d) Plot of absorbance intensity of ET-BDP-O NPs at 592 nm, with storage in water for different days. (e) Fluorescence spectra of ET-BDP-O in THF/H_2O mixture with different water fractions (0–90% v/v). (f) Plot of relative peak intensity versus the composition of the THF/H_2O mixtures of ET-BDP-O.

300 nm to 800 nm. The ET-BDP-O displayed two characteristic absorption peaks at 351 nm and 592 nm. Although assembling into aggregate structure, the ET-BDP-O NPs in water still exhibited a similar absorption pattern compared with free ET-BDP-O in aqueous solution. For the fluorescence spectra, both of the ET-BDP-O and ET-BDP-O NPs revealed the same characteristic emission peak at 667 nm with excitation wavelength of 600 nm (Fig. 3(b)). These results indicated that the aggregation of ET-BDP-O had no obvious influence on its UV–Vis absorption and fluorescence spectra. In addition, we also monitored the UV–Vis absorption spectra of ET-BDP-O NPs in aqueous solution at different time intervals. As depicted in Figs. 3(c) and 3(d), the absorption spectrum of ET-BDP-O NPs storied for 6 days had no significant decline, which further demonstrated the good stability of ET-BDP-O NPs that was consistent with the D_H analysis in Fig. 2(d).

Furthermore, we investigated the AIE performance of ET-BDP-O by monitoring its fluorescence emission spectra from 600 nm to 800 nm upon addition of different amounts of water in THF. The relative fluorescence intensity at 667 nm with a varying water fraction was also calculated and profiled. As shown in Figs. 3(e) and 3(f), the fluorescence intensity decreased gradually along with the rise of water fraction from 0% to 40%, which was attributed to the twisted intramolecular charge transfer effect.[29] When the water fraction increased to 50–70% that causes the aggregation of ET-BDP-O molecules, the restricted intramolecular rotation movement could induce intensified fluorescence emission signal, exhibiting a typical AIE characteristic.[30] However, the fluorescence intensity became weakened obviously when the water fraction was over 70%, which can be explained as the simultaneous formation of crystalline particles and amorphous particles in the solution. The crystalline

particles would contribute to the enhanced fluorescence intensity, but the amorphous particles do not.[31,32] Overall, these results demonstrated that ET-BDP-O had an excellent AIE performance with a huge potential for bioluminescence imaging.

3.4. *ROS generation*

EPR was conducted to detect the $^1O_2$ generation via spin trap TEMP. As shown in Fig. 4(a), the characteristic signal of spin adduct TEMPO (specially generated from the oxidation of $^1O_2$) with a peak intensity ratio of 1:1:1 increased significantly when the ET-BDP-O NPs dispersed in water (aggregated state) were irradiated under 592 nm LED light, demonstrating the excellent light-activated $^1O_2$ generation capacity. However, when the ET-BDP-O was molecularly dissolved in THF solution (molecular state), the intensity of characteristic peaks only had moderate increase. Besides, we also

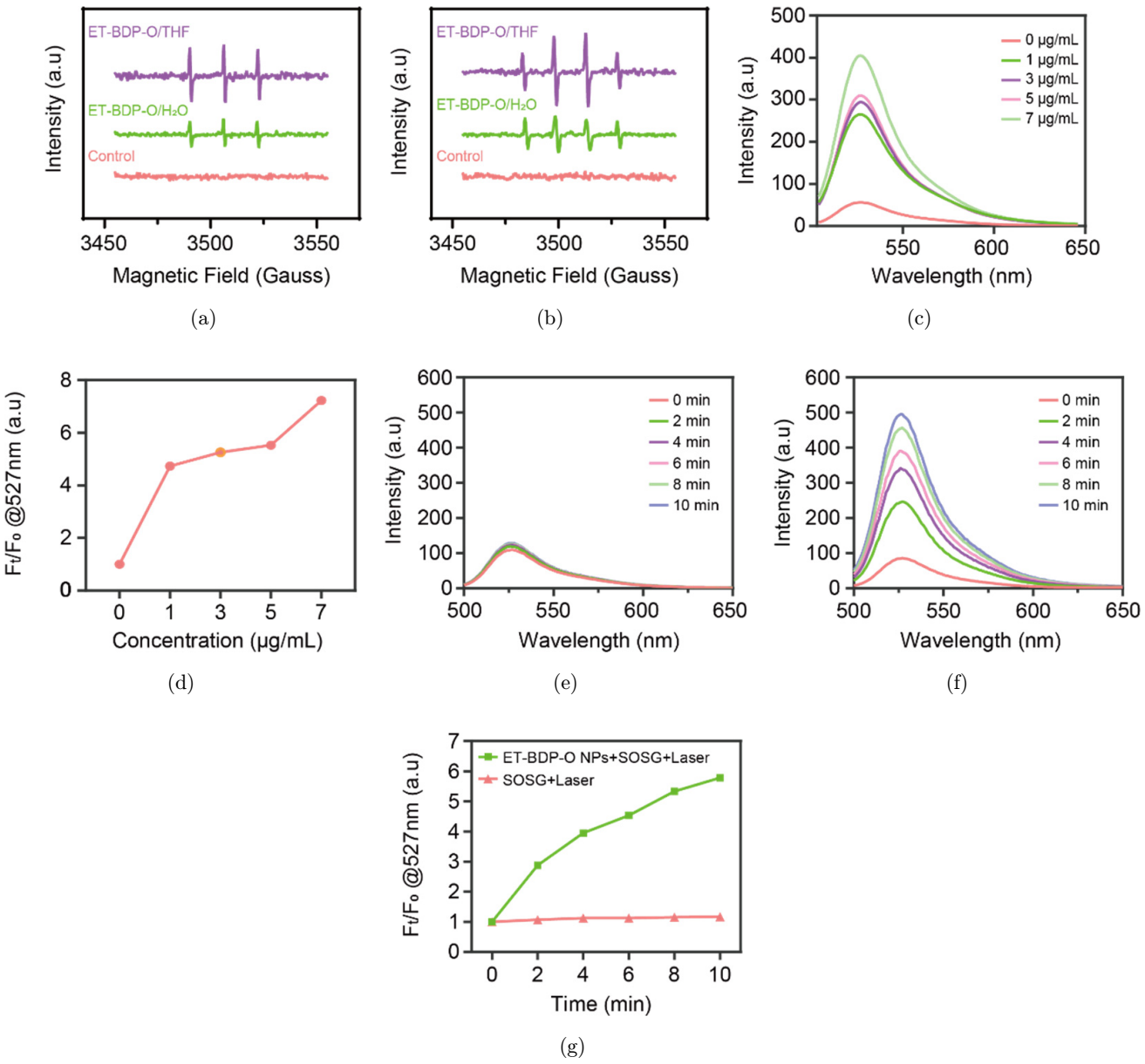

Fig. 4. (a) EPR spectra of $^1O_2$ trapped by TEMP. (b) EPR spectra of hydroxyl radical trapped by DMPO. (c) Fluorescence spectra of SOSG in the presence ET-BDP-O NPs with different concentrations under 592 nm LED light (60 mW/cm^2) for 10 min. (d) The relative fluorescence intensity of SOSG at 527 nm corresponding to (c). (e) and (f) Fluorescence spectra of SOSG in the absence or presence of ET-BDP-O NPs under 592 nm LED light (60 mW/cm^2) for different times. (g) The relative fluorescence intensity of SOSG at 527 nm corresponding to (e) and (f).

monitored the hydroxyl radical (·OH) production of ET-BDP-O using EPR spectra via spin trap DMPO (Fig. 4(b)). The enhanced characteristic 1:2:2:1 four-line signal of DMPO/·OH adduct indicated that ET-BDP-O could also produce ·OH in the process of photoactivation. Especially, the aggregated state of ET-BDP-O had a stronger increase in the characteristic peaks as the same trend as the $^1O_2$ generation in Fig. 4(a), both providing direct evidence that ET-BDP-O in aggregated state possessed enhanced ROS generation ability.

To further evaluate the photodynamic effect of ET-BDP-O NPs, SOSG agent as a detection probe was also utilized to monitor the generation of singlet oxygen.[33] After irradiation under 592 nm LED light (60 mW/cm^2) for 10 min, the fluorescence spectra of SOSG in the solution containing different concentrations of ET-BDP-O NPs were measured and the relative fluorescence intensity (F_t/F_0) was calculated. As depicted in Figs. 4(c) and 4(d), a striking increase of fluorescence intensity of SOSG could be observed along with the concentration of ET-BDP-O NPs. Meanwhile, we also found that the ET-BDP-O NPs (7 μg/mL) exhibited a time-dependent trend of $^1O_2$ generation reflected by the increase of fluorescence intensity (Figs. 4(e) and 4(f)). Besides, the relative fluorescence intensity at 527 nm increased more than five times with the irradiation for 10 min (Fig. 4(g)), and the pattern showed a nearly linear dependence on the irradiation time, demonstrating outstanding photostability for continuous $^1O_2$ production. Taken together, these results illustrate ET-BDP-O NPs have an excellent $^1O_2$ generation ability for potential PDT usage.

3.5. *Cellular uptake and fluorescence imaging in vitro*

The cellular uptake of ET-BDP-O NPs was evaluated prior to phototherapy *in vitro*. The cellular uptake behavior of ET-BDP-O NPs could be clearly observed and imaged under a CLSM rely on the excellent AIE characteristic. As shown in Fig. 5,

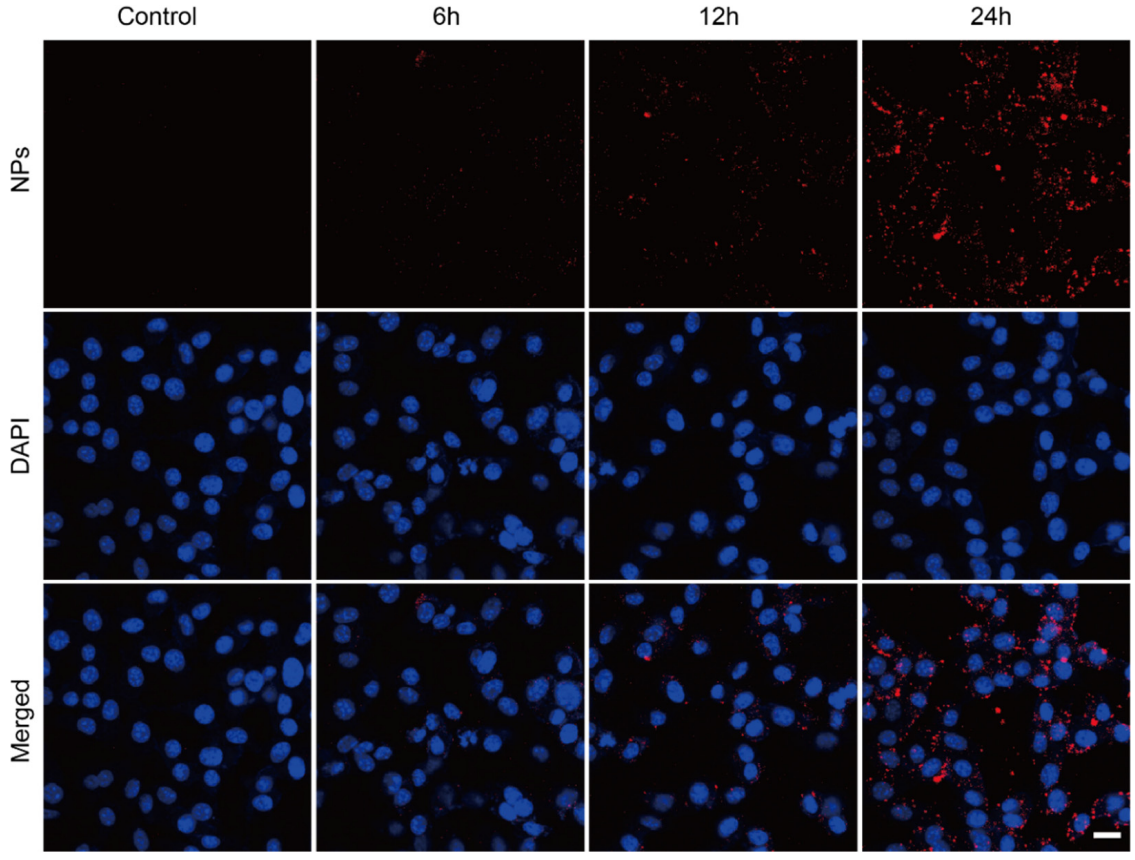

Fig. 5. Cellular uptake of ET-BDP-O NPs by 4T1 cells. CLSM images of 4T1 cells incubated with ET-BDP-O NPs for 6, 12 and 24 h. Cell nuclei stained with DAPI were indicated as the blue fluorescence, while ET-BDP-O NPs indicated as red fluorescence. Scale bars: 50 μm.

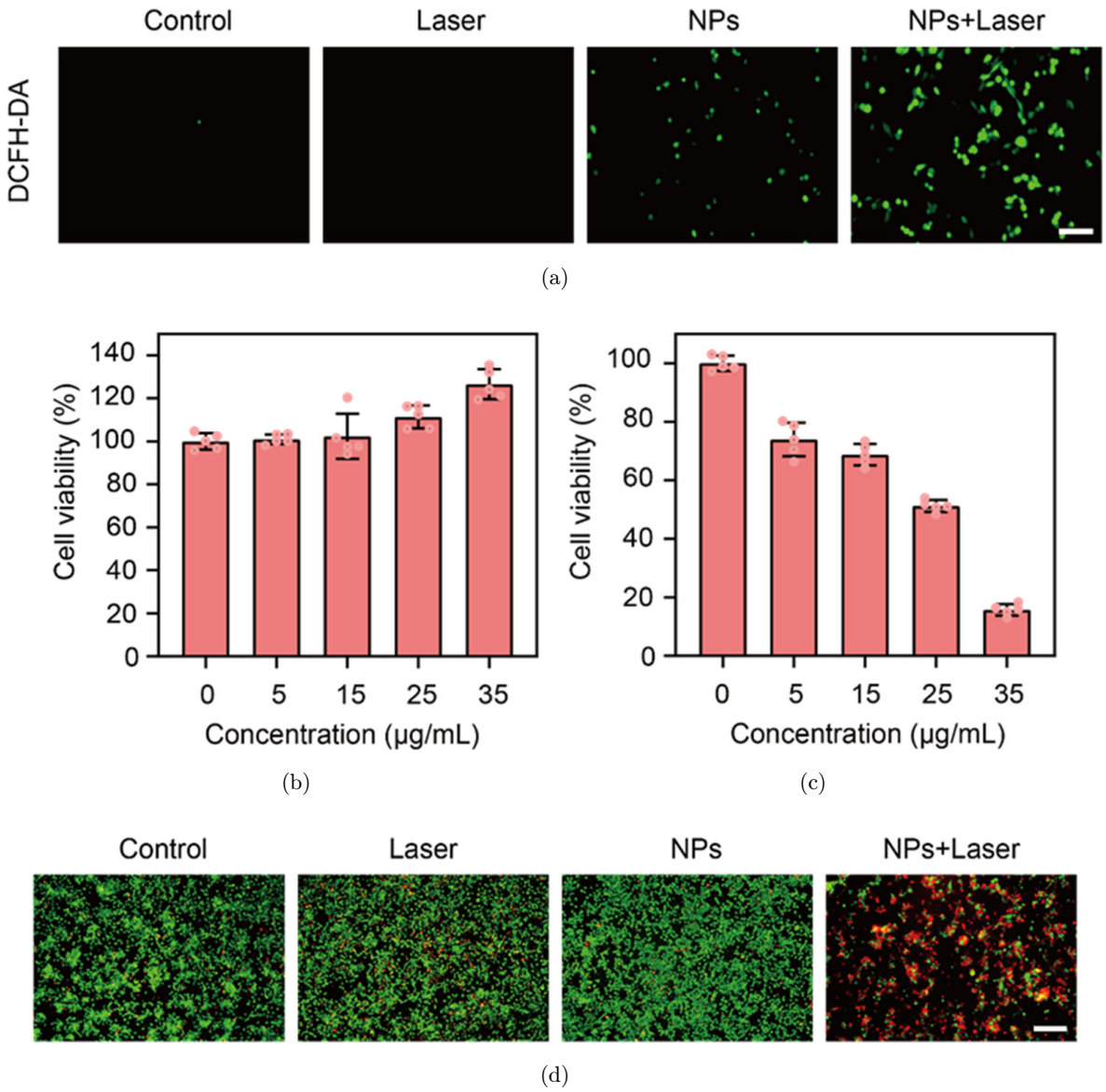

Fig. 6. The *in vitro* ROS generation and photodynamic killing efficacy of ET-BDP-O NPs. (a) Fluorescence images of ROS detection probe of DCFH-DA in 4T1 cells with different treatments. Scale bar: 100 μm. (b) The cell viability of 4T1 cells treated with ET-BDP-O NPs at different concentrations without light irradiation. (c) The cell viability of 4T1 cells treated with ET-BDP-O NPs at different concentrations with light irradiation (60 mW/cm^2, 10 min). (d) Fluorescence images of Calcein-AM/PI-stained 4T1 cells with different treatments. Scale bar: 200 μm.

with the extension of co-incubation time, the red fluorescence of ET-BDP-O NPs increasingly accumulated at the cytoplasm and perinuclear region of 4T1 cells, which showed the strongest red fluorescence signal at 24 h of incubation. These results not only demonstrated the efficient internalization of ET-BDP-O NPs into 4T1 cells, but also showed a bright fluorescence imaging of cells benefited from the AIE characteristics.

3.6. *Intracellular ROS detection*

Intracellular ROS generation of ET-BDP-O NPs was assessed via DCFH-DA probe, which can emit intense green fluorescent signal in the present of intracellular ROS.[34] As shown in Fig. 6(a), there was almost negligible green fluorescence signal when the cells treated with only light irradiation. However, a small amount of green fluorescence could be observed in the cells incubated with ET-BDP-O

NPs alone, ascribing to the stimulation of ET-BDP-O NPs by external natural light. Most significantly, when the cells were treated with ET-BDP-O NPs and followed LED light irradiation ($60\,mW/cm^2$) for 10 min, amount of ROS production in 4T1 cells indicated by the strongest green fluorescence signal, illustrating the excellent ROS generation performance of ET-BDP-O NPs upon light irradiation.

3.7. *Photodynamic effect in vitro*

Subsequently, we explored the photodynamic killing effect of ET-BDP-O NPs against 4T1 cells *in vitro* using CCK-8 assay. As shown in Figs. 6(b) and 6(c), 4T1 cells still maintained over 95% survival rate after incubation with ET-BDP-O NPs at a high concentration of 35 μg/mL for 24 h under dark conditions, suggesting the negligibly dark cytotoxicity. Once exposed to the light irradiation ($60\,mW/cm^2$, 10 min) after ET-BDP-O NPs treatment, the cell viability of 4T1 cells was negatively correlated with the concentration of ET-BDP-O NPs, and only 15% of 4T1 cells survived when the concentration of NPs reached 35 μg/mL.

Additionally, the killing effect of ET-BDP-O NPs was further investigated using live/death cell staining assay. The 4T1 cells treated with different conditions (control, ET-BDP-O NPs, light irradiation and ET-BDP-O NPs + light irradiation) were stained with Calcein-AM and PI, then imaged under a fluorescence microscope, where the green fluorescence represented viable cells and the red fluorescence represented dead cells (Fig. 6(d)). When the cells treated with ET-BDP-O NPs and light irradiation, the viable cells sharply decreased along with a significant increase of dead cells compared with control group, while either only incubated with ET-BDP-O NPs or only light irradiation had little influence on cell survival. These results were consistent with the CCK-8 assay, both demonstrating the as-prepared ET-BDP-O NPs possessed excellent photo-triggered cytotoxicity and could serve as a photodynamic agent with great potential for further bio-application.

4. Conclusions

In summary, we have successfully designed and synthesized a novel AIE-based PS (ET-BDP-O) with D–A–D molecular structure by linking the two liner arms of BODIPY core with TPA units. The further formed ET-BDP-O NPs via direct self-assembly without any other ingredients boasted excellent colloid stability, photostability and AIE photophysical characteristics. After internalized by 4T1 cancer cells, ET-BDP-O NPs were found to emit bright fluorescence for imaging and elevate intracellular ROS level to effectively kill cancer cells for PDT under LED light irradiation. This work proved the great potential of ET-BDP-O NPs as an AIE-based photodynamic agent for fluorescence imaging-guided PDT and deserve for further exploration *in vivo*. However, light activated PDT against deep tumor is always hindered by the shallow penetration. To resolve this problem, recent literatures report that other stimulation sources like microwave and X-ray with deep tissue penetration can be also used to trigger sensitizers for ROS generation,[34–36] which might be also incorporated in ET-BDP-O NPs in our future work.

Conflicts of Interest

There are no conflicts to declare.

Acknowledgments

This work is supported by the National Natural Science Foundation of China (Grant No. 81871483); the Medical Innovation Project of Fujian Province (Grant No. 2021CXA030).

References

1. A. E. O'Connor, W. M. Gallagher, A. T. Byrne, "Porphyrin and nonporphyrin photosensitizers in oncology: Preclinical and clinical advances in photodynamic therapy," *Photochem. Photobiol.* **85**, 1053–1074 (2009).
2. Q. Zhang, J. He, W. Yu, Y. Li, Z. Liu, B. Zhou, Y. Liu, "A promising anticancer drug: A photosensitizer based on the porphyrin skeleton," *RSC Med. Chem.* **11**, 427–437 (2020).
3. P. Agostinis, K. Berg, K. A. Cengel, T. H. Foster, A. W. Girotti, S. O. Gollnick, S. M. Hahn, M. R. Hamblin, A. Juzeniene, D. Kessel, M. Korbelik, J. Moan, P. Mroz, D. Nowis, J. Piette, B. C. Wilson, J. Golab, "Photodynamic therapy of cancer: An update," *CA, Cancer J. Clin.* **61**, 250–281 (2011).
4. O. J. Fakayode, N. Tsolekile, S. P. Songca, O. S. Oluwafemi, "Applications of functionalized

nanomaterials in photodynamic therapy," *Biophys. Rev.* **10**, 49–67 (2018).
5. E. J. Hong, D. G. Choi, M. S. Shim, "Targeted and effective photodynamic therapy for cancer using functionalized nanomaterials," *Acta Pharm. Sin. B* **6**, 297–307 (2016).
6. Z. Zhou, J. Song, L. Nie, X. Chen, "Reactive oxygen species generating systems meeting challenges of photodynamic cancer therapy," *Chem. Soc. Rev.* **45**, 6597–6626 (2016).
7. S. Liu, G. Feng, B. Z. Tang, B. Liu, "Recent advances of AIE light-up probes for photodynamic therapy," *Chem. Sci.* **12**, 6488–6506 (2021).
8. H. Abrahamse, M. R. Hamblin, "New photosensitizers for photodynamic therapy," *Biochem. J.* **473**, 347–364 (2016).
9. M. A. Rajora, J. W. H. Lou, G. Zheng, "Advancing porphyrin's biomedical utility via supramolecular chemistry," *Chem. Soc. Rev.* **46**, 6433–6469 (2017).
10. M. Lan, S. Zhao, W. Liu, C. Lee, W. Zhang, P. Wang, "Photosensitizers for photodynamic therapy," *Adv. Healthc. Mater.* **8**, 1900132 (2019).
11. J. J. Schuitmaker, P. Baas, H. L. V. Leengoed, F. W. V. D. Meulen, W. M. Star, N. V. Zandwijk, "Photodynamic therapy: A promising new modality for the treatment of cancer," *J. Photochem. Photobiol. B* **34**, 3–12 (1996).
12. A. Juzeniene, Q. Peng, J. Moan, "Milestones in the development of photodynamic therapy and fluorescence diagnosis," *Photochem. Photobiol. Sci.* **6**, 1234–1245 (2007).
13. H. Chen, Y. Qiu, D. Ding, H. Lin, W. Sun, G. D. Wang, W. Huang, W. Zhang, D. Lee, G. Liu, J. Xie, X. Chen, "Gadolinium-encapsulated graphene carbon nanotheranostics for imaging-guided photodynamic therapy," *Adv. Mater.* **30**, 1802748 (2018).
14. J. Tian, B. Huang, M. Hasnainnawaz, W. Zhang, "Recent advances of multi-dimensional porphyrin-based functional materials in photodynamic therapy," *Coord. Chem. Rev.* **420**, 213410 (2020).
15. A. Loudet, K. Burgess, "BODIPY dyes and their derivatives: Syntheses and spectroscopic properties," *Chem. Rev.* **107**, 4891–4932 (2007).
16. J. Zhang, N. Wang, X. Ji, Y. Tao, J. Wang, W. Zhao, "BODIPY-based fluorescent probes for biothiols," *Chem. Eur. J.* **26**, 4172–4192 (2020).
17. N. Boens, V. Leen, W. Dehaen, "Fluorescent indicators based on BODIPY," *Chem. Soc. Rev.* **41**, 1130–1172 (2012).
18. L. Antina, A. A. Ksenofontov, A. Kazak, T. Usol, M. B. Berezin, "Effect of ms-substitution on aggregation behavior and spectroscopic properties of BODIPY dyes in aqueous solution, Langmuir-Schaefer and poly(methyl methacrylate) thin films," *Colloids Surf. A, Physicochem. Eng. Aspects* **618**, 126449 (2021).
19. S. Radunz, E. Andresen, C. Würth, A. Koerdt, U. Resch-Genger, "Simple self-referenced luminescent pH sensors based on upconversion nanocrystals and pH-sensitive fluorescent BODIPY dyes," *Anal. Chem.* **91**, 7756–7764 (2019).
20. M. Zhu, P. Xing, Y. Zhou, L. Gong, J. Zhang, D. Qi, Y. Bian, H. Du, J. Jiang, "Lysosome-targeting ratiometric fluorescent pH probes based on long-wavelength BODIPY," *J. Mater. Chem. B* **6**, 4422–4426 (2018).
21. Y. Chen, W. Ai, X. Guo, Y. Li, Y. Ma, L. Chen, H. Zhang, T. Wang, X. Zhang, Z. Wang, "Mitochondria-targeted polydopamine nanocomposite with AIE photosensitizer for image-guided photodynamic and photothermal tumor ablation," *Small* **15**, 1902352 (2019).
22. J. Xie, Y. Wang, W. Choi, P. Jangili, Y. Ge, Y. Xu, J. Kang, L. Liu, B. Zhang, Z. Xie, J. He, N. Xie, G. Nie, H. Zhang, J. S. Kim, "Overcoming barriers in photodynamic therapy harnessing nano-formulation strategies," *Chem. Soc. Rev.* **50**, 9152–9201 (2021).
23. R. Bonnett, "Photosensitizers of the porphyrin and phthalocyanine series for photodynamic therapy," *Chem. Soc. Rev.* **24**, 19–33 (1995).
24. X. F. Zhang, "BisBODIPY as PCT-based halogen free photosensitizers for highly efficient excited triplet state and singlet oxygen formation: Tuning the efficiency by different linking positions," *Dyes Pigments* **146**, 491–501 (2017).
25. W. Wang, F. Wu, Q. Zhang, N. Zhou, M. Zhang, T. Zheng, Y. Li, B. Z. Tang, "Aggregation-induced emission nanoparticles for single near-infrared light-triggered photodynamic and photothermal antibacterial therapy," *ACS Nano* **16**, 7961–7970 (2022).
26. M. Yang, J. Deng, H. Su, S. Gu, J. Zhang, A. Zhong, F. Wu, "Small organic molecule-based nanoparticles with red/near-infrared aggregation-induced emission for bioimaging and PDT/PTT synergistic therapy," *Mater. Chem. Front.* **5**, 406–417 (2021).
27. M. Hussain, A. M. El-Zohry, H. B. Gobeze, J. Zhao, F. D'Souza, O. F. Mohammed, "Intramolecular energy and electron transfers in bodipy naphthalene-diimide triads," *J. Phys. Chem. A* **122**, 6081–6088 (2018).
28. Z. Xiong, X. Zhang, L. Liu, Q. Zhu, Z. Wang, H. Feng, Z. Qian, "Achieving highly efficient aggregation-induced emission, reversible and irreversible photochromism by heavy halogen-regulated photophysics and D-A molecular pattern-controlled photochemistry of through-space conjugated luminogens," *Chem. Sci.* **12**, 10710–10723 (2021).

29. Y. Xu, C. Li, R. Xu, N. Zhang, Z. Wang, X. Jing, Z. Yang, D. Dang, P. Zhang, L. Meng, "Tuning molecular aggregation to achieve highly bright AIE dots for NIR-II fluorescence imaging and NIR-I photoacoustic imaging," *Chem. Sci.* **11**, 8157–8166 (2020).
30. W. Che, G. Li, J. Zhang, Y. Geng, Z. Xie, D. Zhu, Z. Su, "Exploiting aggregation induced emission and twisted intramolecular charge transfer in a BODIPY dye for selective sensing of fluoride in aqueous medium and living cells," *J. Photochem. Photobiol. A* **358**, 274–283 (2018).
31. J. Yang, G. Li, W. Che, Y. Liu, M. R. Bryce, "A neutral dinuclear Ir(III) complex for anti-counterfeiting and data encryption," *Chem. Commun.* **53**, 3022–3025 (2017).
32. W. Shao, C. Yang, F. Li, J. Wu, N. Wang, Q. Ding, J. Gao, D. Ling, "Molecular design of conjugated small molecule nanoparticles for synergistically enhanced PTT/PDT," *Nano-Micro Lett.* **12**, 147 (2020).
33. X. Cai, B. Liu, M. Pang, J. Lin, "Interfacially synthesized Fe-soc-MOF nanoparticles combined with ICG for photothermal/photodynamic therapy," *Dalton Trans.* **47**, 16329–16336 (2018).
34. N. K. Pandey, W. Xiong, L. Wang, W. Chen, B. Bui, J. Yang, E. Amador, M. Chen, C. Xing, A. A. Athavale, Y. Hao, W. Feizi, L. Lumata, "Aggregation-induced emission luminogens for highly effective microwave dynamic therapy," *Bioact. Mater.* **7**, 112–125 (2022).
35. X. Chen, J. Liu, Y. Li, N. K. Pandey, T. Chen, L. Wang, E. H. Amador, W. Chen, F. Liu, E. Xiao, W. Chen, "Study of copper-cysteamine based X-ray induced photodynamic therapy and its effects on cancer cell proliferation and migration in a clinical mimic setting," *Bioact. Mater.* **7**, 504–514 (2022).
36. S. Shrestha, J. Wu, B. Sah, A. Vanasse, L. N. Cooper, L. Ma, G. Li, H. Zheng, W. Chen, M. P. Antosh, "X-ray induced photodynamic therapy with copper-cysteamine nanoparticles in mice tumors," *Proc. Natl. Acad. Sci. USA* **116**, 16823–16828 (2019).